monitor SF using both arbitrarily sized cylindrical phantoms and short acquisition times, making the method particularly useful for daily QC purposes.

[a]Author to whom correspondence should be addressed. Electronic mail: h.w.a.m.dejong@umcutrecht.nl; Telephone: +31-(0)88-7553327.

[1]G. Brix *et al.*, "Performance evaluation of a whole-body PET scanner using the NEMA protocol," J. Nucl. Med. **38**, 1614–1623 (1997).

[2]National Manufacturers Association, NEMA Standards Publication No. NU 2-1994 (National Manufacturers, Washington, DC, 1994).

[3]M. E. Daube-Witherspoon *et al.*, "PET performance measurements using the NEMA NU 2-2001 standard," J. Nucl. Med. **43**, 1398–1409 (2002).

[4]H. Herzog, L. Tellmann, C. Hocke, U. Pietrzyk, M. E. Casey, and T. Kuwert, "NEMA NU2-2001 guided performance evaluation of four Siemens ECAT PET scanners," IEEE Trans. Nucl. Sci. **51**, 2662–2669 (2004).

[5]National Manufacturers Association, NEMA Standards Publication No. NU 2-2001 (National Electrical Manufacturers, Washington, DC, 2001).

[6]National Manufacturers Association, NEMA Standards Publication No. NU 2-2007 (National Electrical Manufacturers, Washington, DC, 2007).

[7]E. J. Hoffman, S. C. Huang, M. E. Phelps, and D. E. Kuhl, "Quantitation in positron emission computed tomography: 4. Effect of accidental coincidences," J. Comput. Assist. Tomogr. **5**, 391–400 (1981).

[8]C. de Boor, *A Practical Guide to Splines* (Springer-Verlag, New York, 1978).

[9]D. Marquardt, "An algorithm for least-squares estimation of nonlinear parameters," SIAM J. Appl. Math. **11**, 431–441 (1963).

[10]C. C. Watson, M. E. Casey, L. Eriksson, T. Mulnix, D. Adams, and B. Bendriem, "NEMA NU 2 performance tests for scanners with intrinsic radioactivity," J. Nucl. Med. **45**, 822–826 (2004).

[11]H. W. de Jong, F. H. van Velden, R. W. Kloet, F. L. Buijs, R. Boellaard, and A. A. Lammertsma, "Performance evaluation of the ECAT HRRT: An LSO-LYSO double layer high resolution, high sensitivity scanner," Phys. Med. Biol. **52**, 1505–1526 (2007).

[12]K. Wienhard *et al.*, "The Ecat exact HR—Performance of a new high-resolution positron scanner," J. Comput. Assist. Tomogr. **18**, 110–118 (1994).

[13]S. Surti and J. S. Karp, "Imaging characteristics of a 3-dimensional GSO whole-body PET camera," J. Nucl. Med. **45**, 1040–1049 (2004).

[14]J. S. Kim *et al.*, "Performance measurement of the microPET Focus 120 scanner," J. Nucl. Med. **48**, 1527–1535 (2007).

[15]National Manufacturers Association, "Performance measurements of small animal positron emission tomographs," NEMA Standards Publication No. NU 2-2008 (National Electrical Manufacturers, Washington, DC, 2008).

[16]Y. C. Tai *et al.*, "Performance evaluation of the microPET Focus: A third-generation microPET scanner dedicated to animal imaging," J. Nucl. Med. **46**, 455–463 (2005).

[17]C. C. Watson, "New, faster, image-based scatter correction for 3D PET," IEEE Trans. Nucl. Sci. **47**, 1587–1594 (2000).

[18]M. Lubberink, S. A. van, H. W. de Jong, G. A. van Dongen, and G. J. Teule, "Acquisition settings for PET of 124I administered simultaneously with therapeutic amounts of 131I," J. Nucl. Med. **47**, 1375–1381 (2006).

Eur J Nucl Med Mol Imaging (2009) 36:2014–2026
DOI 10.1007/s00259-009-1140-y

ORIGINAL ARTICLE

Non-invasive estimation of hepatic glucose uptake from [^{18}F] FDG PET images using tissue-derived input functions

N. Kudomi · M. J. Järvisalo · J. Kiss · R. Borra · A. Viljanen · T. Viljanen · T. Savunen · J. Knuuti · H. Iida · P. Nuutila · P. Iozzo

Received: 4 August 2008 / Accepted: 2 April 2009 / Published online: 13 June 2009

Abstract
Purpose The liver is perfused through the portal vein and hepatic artery. Quantification of hepatic glucose uptake (HGU) using PET requires the use of an input function for both the hepatic artery and portal vein. The former can be generally obtained invasively, but blood withdrawal from the portal vein is not practical in humans. The aim of this study was to develop and validate a new technique to obtain quantitative HGU by estimating the input function from PET images.
Methods Normal pigs (n=12) were studied with [^{18}F]FDG PET, in which arterial and portal blood time-activity curves (TAC) were determined invasively to serve as reference measurements. The present technique consisted of two characteristics, i.e. using a model input function and simultaneously fitting multiple liver tissue TACs from images by minimizing the residual sum of square between the tissue TACs and fitted curves. The input function was obtained from the parameters determined from the fitting. The HGU values were computed by the estimated and measured input functions and compared between the methods.
Results The estimated input functions were well reproduced. The HGU values, ranging from 0.005 to 0.02 ml/min per ml, were not significantly different between the two methods (r=0.95, p<0.001). A Bland-Altman plot demonstrated a small overestimation by the image-derived method with a bias of 0.00052 ml/min per g for HGU.
Conclusion The results presented demonstrate that the input function can be estimated directly from the PET image, supporting the fully non-invasive assessment of liver glucose metabolism in human studies.

Keywords [^{18}F]FDG PET · [^{18}F]FDG uptake kinetic modelling · Hepatic glucose uptake · Non-invasive · Input function

N. Kudomi (✉) · M. J. Järvisalo · R. Borra · A. Viljanen · T. Viljanen · J. Knuuti · P. Nuutila · P. Iozzo
Turku PET Centre, University of Turku,
P.O. Box 52, 20521 Turku, Finland
e-mail: nobuyuki.kudomi@tyks.fi

J. Kiss · T. Savunen
Department of Surgery, University of Turku,
Turku, Finland

H. Iida
Department of Investigative Radiology,
Advanced Medical Engineering Center,
National Cardiovascular Center-Research Institute,
5-7-1, Fujishirodai,
Suita, Osaka 565-8565, Japan

P. Nuutila
Department of Medicine, University of Turku,
Turku, Finland

P. Iozzo
Institute of Clinical Physiology, National Research Council,
56100 Pisa, Italy

Introduction

Abnormalities in hepatic glucose uptake (HGU) have been implicated in the pathogenesis of liver steatosis, hypertriglyceridaemia and diabetes [2, 6, 10]. Thus, HGU may become a prognostic indicator and useful marker during progression or treatment follow-up. Positron emission tomography (PET) in combination with [^{18}F]fluorodeoxyglucose ([^{18}F]FDG) is a potential tool to assess HGU, as shown by us and others in humans [4, 11] and animals [13, 18].

The liver is characterized by a dual blood supply, comprising the hepatic artery and the portal vein, draining

venous blood from the gastrointestinal tract. Thus, in the modelling of PET data from liver, two blood time-activity curves (TAC) are required to represent the input function. We have previously validated a technique for quantification of HGU against organ balance measurements in large animals, by using arterial and portal blood sampling [13]. However, in humans the portal vein cannot be accessed, and even blood withdrawal from a peripheral artery [5, 15, 16, 23, 27] is not always successful or not risk free, and it requires careful correction in time delay between the sampling site and the tissue [8, 9]. It follows that obtaining quantitative data on the hepatic dual input function in humans by a non-invasive approach such as an image-derived method would optimize patient safety together with the quality of results.

We have recently reported a new method in which the arterial and portal inputs were estimated from multiple tissue TACs in the quantification of hepatic blood flow using $H_2{}^{15}O$ [17]. In the present study, we adapted the method to liver [^{18}F]FDG data (collected during our previous study [12, 13]). The method is characterized by use of a model input function, which is used to create a tissue model function based on the known kinetics of the tracer in the liver. Then the created model tissue function is used to simultaneously fit multiple tissue curves. To estimate the input function for the liver [^{18}F]FDG data, the shape of the input curve and also the kinetic model of tracer in the liver tissue are different as compared to those of $H_2{}^{15}O$, thus the validity of the model-based method has to be tested. We tested its validity in the assessment of HGU under fasting and insulin-stimulated conditions in pigs undergoing invasive blood sampling together with PET imaging.

Materials and methods

Theory and computation of non-invasive input function

A model function was introduced as the input function in the mixed form, resulting from hepatic artery and portal vein curves. First, a model function was created to shape the [^{18}F]FDG input function. The model function introduced ($C_I(t)$) was expressed as:

$$
\begin{aligned}
C_I(t) &= 0. && (t < t_1)\\
&= A\left[\frac{1-\exp(\beta(t_1-t))}{\beta}+\frac{\alpha(1-\exp(\beta(t_1-t)))}{a(1-a)\beta}-\frac{\alpha(\exp(K_E(1-a)(t_1-t_2))-\exp(\beta(t_1-t)))}{a(1-a)\gamma}\right] && (t_1 < t < t_2)\\
&= A\left[\begin{array}{l}\frac{\exp(\beta(t_2-t))-\exp(\beta(t_1-t))}{\beta}+\frac{\alpha(1-\exp(\beta(t_1-t_2)))}{a(1-a)\beta}+\frac{\alpha(\exp(K_E\beta(t_1-t_2))-\exp(\beta(t_1-t_2)))}{a(1-a)\gamma}\\ +\frac{\alpha(\exp(K_E(1-a)t_2)-\exp(K_E(1-a)t_1))(\exp(K_E(1-a)t)-\exp(\gamma t_2-\beta t)))}{a(1-a)\gamma}\end{array}\right] && (t > t_2)\\
\alpha &= K_I/K_E, \quad \beta = K_E + K_I/a, \quad \gamma = aK_E + K_I/a\\
a &= (\alpha - 1 + K_M/K_E)/2 + \sqrt{\alpha + (\alpha - 1 + K_M/K_E)^2}\Big/4
\end{aligned}
\tag{1}
$$

Details of derivation of this model function are given in the "Appendix" section. Briefly, the model function was created by assuming a three-compartment model in which the tracer is administered in a rectangular form, it diffuses bidirectionally between arterial and whole body peripheral tissue (second compartment) and is in part metabolized and accumulated in the third compartment. A is a scalar parameter reflecting the given amount of tracer, and t_1 and t_2- t_1 represent the appearance time of the tracer and the duration of administration. K_E (ml/min) and K_I (ml/min) represent the tracer bidirectional diffusion rates between arterial blood and whole-body interstitial spaces, respectively, and K_M (ml/min) represents the tracer metabolic rate in the assumed whole-body compartment (i.e. the rate constant from second to third compartment).

Using the model function, the tissue response function for the tracer can be expressed by applying a two-tissue compartment model (in this report, 'two-tissue compartment model' is used to express kinetics of [^{18}F]FDG in hepatic tissue and 'three-compartment model' is used to shape the model function of the input), assuming [^{18}F]FDG metabolites as irreversible in hepatic tissue:

$$
\begin{aligned}
C_{Tis}(t) &= h(t) \otimes C_I(t)\\
h(t) &= \frac{K_1}{k_2+k_3}\left(k_3 + k_2 e^{-(k2+k3)t}\right)
\end{aligned}
\tag{2}
$$

Including the blood volume term in this equation, the model function describing [^{18}F]FDG in the hepatic region measured by PET (C_{PET}) can be expressed as

$$
C_{PET}(t) = (1 - V_0)h(t) \otimes C_I(t) + V_0 C_I(t) \tag{3}
$$

Steps to estimate the input function are simplified in the flow chart in Fig. 1. Multiple tissue TACs from the liver image were used to estimate the input functions. First, the model function in Eq. 3 was individually fitted to tissue TACs by a non-linear fitting method (Powell-Brent mini-

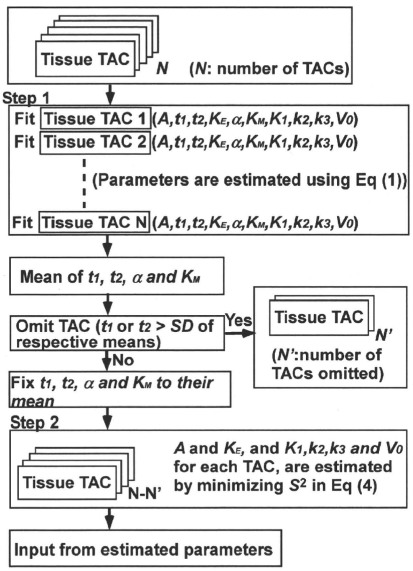

Fig. 1 A schematic diagram of the procedure to estimate the input functions using multiple tissue TACs. *Step 1*: the model function (Eq. 3) was individually fitted to N tissue TACs. Then, means and standard deviations of t_1, t_2, α and K_M were calculated, and the tissue TACs with values of t_1 or t_2>one standard deviation of respective means were excluded (indicated as N' TACs). In the *second step*, assuming that all parts of the liver share the same input functions, values of t_1, t_2, α and K_M were fixed to their means and the other two parameters (A and K_E) were estimated by minimizing Eq. 4 by the grid search method. Finally, the image-based input function was obtained by substituting the estimated parameters into Eq. 1

mization algorithm), and the set of ten parameters, A, t_1, t_2, K_E, α, K_M, K_1, k_2, k_3 and V_0, was obtained for each tissue TAC. Then, means and standard deviations of A, t_1, t_2, K_E, α and K_M were calculated, and the tissue TACs with values of t_1 or t_2>one standard deviation of respective means were excluded to avoid the potential influence of TACs outside the liver. In the second step, assuming that all parts of the liver share the same input function, values of t_1, t_2, α and K_M were fixed to their means and the other two parameters (A and K_E) in the model input function were estimated by minimizing the following equation:

$$S^2 = \sum_{i\in Tis}\sum_{k}\left(C_{Tis}^{i,k} - \left((1-V_0^i)h^i(t)\otimes C_l(t) + V_0^i C_l(t)\right)\right)^2 \quad (4)$$

where $C_{\mathrm{Tis}}^{i,k}$ is the activity concentration for kth frame in ith tissue region of interest, t is the corresponding time of kth frame and $h^i(t)$ is defined as in Eq. 2 with rate constant values of K^i_1, k^i_2 and k^i_3, and blood volume of V_0^i, for ith tissue region, respectively. In this procedure, S^2 was minimized by the grid search method to avoid dependency on initial guess, where S^2 was calculated for 1,000 discrete values of both A and K_E between ranges of three standard deviations from respective mean values, omitting the negative value. In this procedure, for a given input function, i.e. once A and K_E are given, then K^i_1, k^i_2, k^i_3 and V_0^i for ith TAC were computed by the Powell-Brent minimization algorithm, with acceptable ranges of 0–5 ml/min per g, 0–5 min^{-1}, 0–1 min^{-1} and 0–0.5 ml/ml, respectively, and then substituted into Eq. 4. Finally, the image-based input function was obtained by substituting the estimated parameters into Eq. 1.

Simulation study

The influence of noise versus number of TACs on the accuracy of the method was explored. As the noise on tissue TACs increased, the standard deviation of uptake ratio of tracer increased; as more regions were used, the standard deviation tended to decrease. However, if the number of TACs is larger, the noise on tissue is also large and vice versa. Our simulation was intended to reveal an optimal number of tissue TACs to be extracted from the whole region of the liver. First, to this purpose, we selected one mixed input function from one of the present experiments and used it as true input function in this simulation. One of the present experimental data sets was chosen and 100 tissue TACs were extracted as follows: a region of interest (ROI) was placed on the whole area of the liver in a summed image and subsequently divided into 100 subsets of TACs. The subsets were created as follows: first, the area under the curve (AUC) was computed for each pixel TAC. Second, TACs were ordered based on the AUC value and divided into 100 sets. Then, one TAC for each subset was obtained by averaging respective TACs. Each subset consisted of the same number of pixels. The rate constant values and blood volume (K_1, k_2, k_3 and V_0) were computed for each TAC using the corresponding input function by the non-linear Gauss-Newton method, assuming Eq. 3 and parameter values were obtained (means ± SDs were 1.4± 1.0 ml/min per g, 2.1±1.3 min^{-1}, 0.018±0.008 min^{-1} and 0.36±0.12 ml/ml for K_1, k_2, k_3 and V_0, respectively).

Based on the obtained set of rate constant values and blood volume, one set of 100 hepatic tissue TACs was generated from the true input function using Eq. 3. Then, tissue TACs with noise were generated as follows. Gaussian noise at peak was imposed on the set of 100 hepatic tissue TACs. Three levels of noise were introduced, corresponding to 10, 20 and 80% of counts at the level of the peak and 10, 20 and 80% of the square root of counts at the other points.

This procedure was repeated 100 times and 10,000 of noisy tissue TACs, embracing a total of 10,000 pixels, were obtained. Then, the TACs were ordered and averaged with the same procedure as in the experimental study (see below), i.e. the TACs were ordered based on the AUC and divided into N_{tis} (= 10, 15, 20, 50, 100 and 200) groups. The TACs were averaged for each group to obtain N_{tis} TACs. For each N_{tis} and each level of noise, input function was estimated, as described. Then, rate constant values were computed using estimated input function and tissue TACs. This procedure was repeated 100 times and the bias and deviation in values of rate constant values were calculated. Their bias and deviation were presented as a function of N_{tis}.

Experimental study

Study design

Details of the study design are given in previous articles [12, 13]. Briefly, after animal preparation, PET imaging was performed to measure liver glucose uptake during fasting (n=4), physiological (n=4) and supraphysiological (n=4) euglycaemic hyperinsulinaemia. [^{18}F]FDG was injected, and its concentration in the carotid artery and portal vein was frequently measured. Immediately after the animals were sacrificed, the liver was explanted to measure organ density. The protocol was reviewed and approved by the Ethics Committee for Animal Experiments of the University of Turku.

Animal preparation

Twelve anaesthetized, weight-matched pigs were studied during fasting (weight: 29.8±0.6 kg), physiological (1.0 mU · kg^{-1} · min^{-1}; weight: 30.0±0.5 kg) or supraphysiological euglycaemic hyperinsulinaemia (5.0 mU · kg^{-1} · min^{-1}; weight: 30.3±0.5 kg). Animals were deprived of food on the day before the study at 5 p.m. Anaesthesia was induced by injection of 1.0 g ketamine into the neck muscles before transportation of the pigs to the operating room. Throughout the experiment, animals were kept anaesthetized with ketamine and pancuronium (total of 1.5 g and 40 mg, respectively) and mechanically ventilated via tracheal intubation with oxygen and normal room air (regulated ventilation, 16 breaths/min). Catheters were placed in the femoral vein and carotid artery for the administration of glucose, insulin and [^{18}F]FDG and for sampling of arterial blood, respectively. Splanchnic vessels were accessed by subcostal incision; after dissection of the hepatogastric ligament, purse-string sutures were allocated to allow catheter insertion via a small incision in the portal vein. Doppler flow probes were placed around the portal vein and hepatic artery to monitor blood flow [12]. The surgical access was closed, and the distal catheter extremities were secured to the abdominal surface to avoid tip displacement. The animals were then transported to the PET Centre for tracer administration, liver imaging and blood sampling.

PET scanning

Scans were performed using an ECAT 931-08/12 scanner (CTI Inc., Knoxville, TN, USA). After acquisition of a transmission scan to correct for photon attenuation, [^{18}F]FDG (274±7 MBq) was rapidly injected, and an 180-min dynamic [^{18}F]FDG PET scan was started (31 frames, 8×15, 2×30, 2×120, 1×180, 6×300, 8×600 and 4×900 s). We sampled 2 ml of arterial and portal venous blood frequently (i.e. once every imaging time frame) for the determination of plasma [^{18}F]FDG radioactivity. The tube length was 260 mm. To keep tube patency, the line was flushed with a bolus of saline (5 ml), and a slow saline infusion was maintained. Vital signs, blood pressure and heart rate were monitored throughout the study.

Image processing

Dynamic sinogram data were corrected for dead time in each frame in addition to detector normalization. Random counts were also subtracted based on random counting obtained by the off-time coincidence method. Tomographic images were reconstructed from corrected sinogram data by the median root prior reconstruction algorithm (MRP) with 150 iterations and Bayesian coefficient of 0.3 [1]. Scatter correction was not available; however, the MRP can produce more accurate quantitative pixel values with high resolution and good noise reduction than filtered back projection (FBP) or maximum likelihood expectation maximization (MLEM) reconstruction algorithms, and reconstruction artefacts due to the FBP algorithm are reduced [1]. Attenuation correction was applied with transmission data. A reconstructed image had 128×128×15 matrix size with a pixel size of 2.4 mm×2.4 mm and 6.7 mm with 31 frames. Spatial resolution in this scanner is 6.7 mm (axial) and 6.5 mm (in-plane) full-width at half-maximum (FWHM). From this study, the first 60-min data, i.e. 21 frames, were used in the current analysis.

Data processing

Measured arterial ($C_a(t)$ Bq/ml) and portal ($C_p(t)$ Bq/ml) plasma TACs corrected for decay were mixed based on flow rates in hepatic artery (F_a ml/min) and portal vein (F_p ml/min), as determined by the ultrasonography technique, as follows: $(C_a(t)\cdot F_a + C_p(t)\cdot F_p)/(F_a + F_p)$. Then, the mixed

blood curve was corrected for delay by fitting to a whole liver tissue TAC based on a previous method [9], assuming a two-tissue compartment model.

An ROI was placed on the whole region of the liver in a summed image. The ROI for the whole region covered $(1.6\pm0.2)\times10^4$ pixels and was subsequently divided into 30 subsets of TACs. The subsets were created as follows: first, the AUC was computed for each pixel TAC. Second, TACs were ordered based on the AUC value and divided into 30 sets. Then, one TAC for each subset was obtained by averaging respective TACs. Each subset consisted of the same number of pixels. Representative TACs are shown in Fig. 2.

Then, the input function was estimated using TACs in each subset. In the first step, initial values and boundary conditions for the non-linear fitting for each parameter were 20,000 between 0.02 and 200,000,000 Bq/ml for A, 0.30 between 0.1 and 0.5 ml/min for K_E, 10 between −20 and 50 s for t_1, 60 between 50 and 80 s for t_2- t_1, 0.50 between 0.40 and 2.00 for α, 0.085 between 0.05 and 0.50 for K_M, 1.5 between 0.1 and 5 ml/min per g for K_1, 1.5 between 0.1 and 5 min^{-1} for k_2, 0.01 between 0.0001 and 1.0 min^{-1} for k_3 and 0.15 between 0 and 0.5 ml/ml for V_0, respectively. In the second step, the S^2 value in Eq. 4 was minimized, and the image-based input function was obtained. AUC for measured and image-based inputs were calculated for 0–60 min. Their % difference was calculated.

The rate values of K_1, k_2 and k_3 were computed by the non-linear fitting method (Gauss-Newton method) using the equation in combination with either the estimated input function obtained from the present method or blood withdrawal data. Then, hepatic fractional extraction values, $K_i=K_1k_3/(k_2+k_3)$, were calculated and compared between the two methods. Also, K_i values were computed by the Gjedde-Patlak analysis method [7, 21, 22, 26] and values were compared between methods.

Results

Simulation study

Figure 2 compares curves obtained from experimental data and simulated data assuming 10% noise level. They show similar shapes and distributions between the methods, demonstrating that the simulation reproduced experimental conditions.

The influence of noise and the number of tissue TACs, i.e. the size of bias and deviation on overall rate constant values, were minimal when the number of tissue TACs was 10–40 and the influence was independent of noise level (Fig. 3), although the optimal number of tissue TACs depended on the rate constants K_1, k_2, k_3 and K_i. The result suggested that the overall optimal number of tissue TACs to be applied to preserve accuracy is in the above range.

Among the six parameters A, t_1, t_2, K_E, α and K_M, the four parameters t_1, t_2 α and K_M were determined with the same accuracy, i.e. less than 1 s for t_1, less than 5 s for t_2, 5% for α and 7% for K_M, respectively, independent of the number of tissue TACs applied. The degree of deviation of the remaining two parameters depended on the number of parameters.

Experimental study

Reconstructed images are shown in Fig. 4.

The average of estimated delay time between the tissue curve and measured input was 15±13 s.

In the first step, one- or two-tissue TACs were excluded because the estimated t_1 value was smaller than the mean subtracted by one standard deviation. The t_1 value in these TACs were 8–16 s earlier than the mean, suggesting that these TACs were located in a region overlapping the vena cava. The estimated t_2- t_1 was 66±8 s, which was similar to the tracer administration duration.

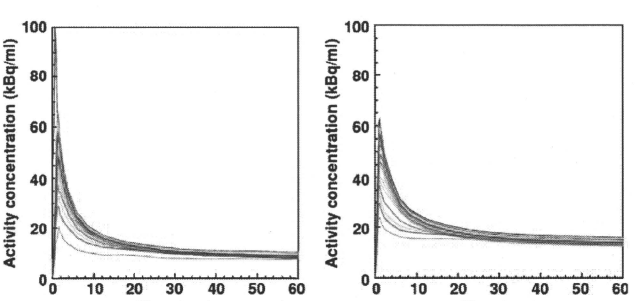

Fig. 2 Comparison of tissue curves obtained from experimental (*left*) and simulated data (*right*), showing similar shapes and distributions between the methods. The *black solid curve* with an extremely large peak in the early phase in the left panel is from a region covering the vena cava, distal to the injection site. The curve was excluded in the first step of the estimation procedure

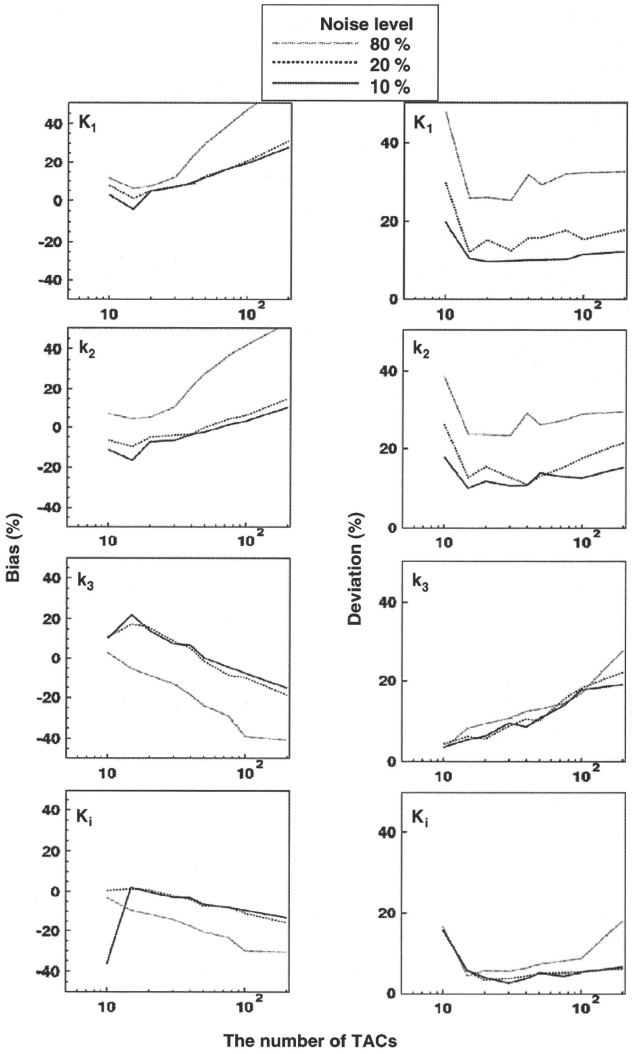

Fig. 3 Bias (*left*) and deviation (*right*) in the rate constant values of K_1, k_2, k_3 and K_i as a function of the number of time activity curves applied to the estimation of the input function

Figure 5 shows a representative fitted curve of the model input function (Eq. 3) directly fitted to the corresponding measured input function, suggesting that the model function was almost fully adequate to estimate the input.

Estimated, image-derived hepatic input functions are shown in Fig. 6. Those were almost identical to the measured curves. The mean ± SD of difference of AUC was −3.6±8.0%, ranging from −10.8 to 12.3%.

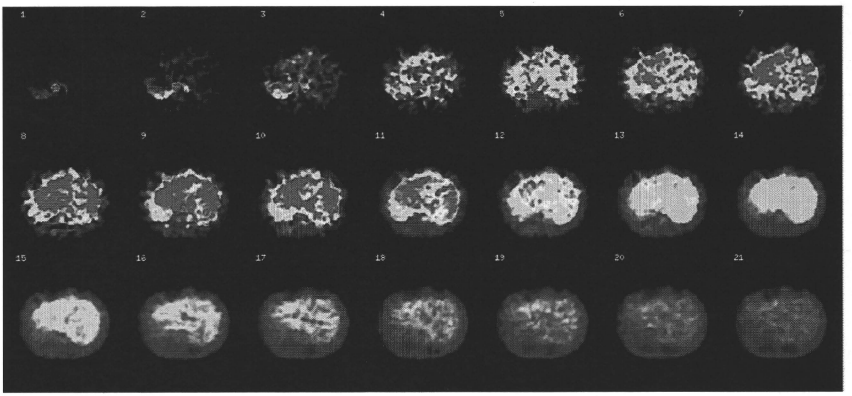

Fig. 4 Representative view of liver [^{18}F]FDG images obtained from one of the experimental studies. Each figure is represented in the same scale and slice at the *n*th frame, which is indicated in the *upper left corner* of each image

The relationships and Bland-Altman plots between values of hepatic K_1, k_2, k_3 and K_i, as estimated by using the image-derived versus the measured blood curves, are shown in Fig. 7. The plots demonstrate a small overestimation by the image-derived method, with a bias of 0.03 and 0.00052 ml/min per g for K_1 and K_i and of −0.043 and 0.00025 min^{-1} for k_2 and k_3, respectively. Respective regression lines were: $y=0.09+0.93x$ ($r=0.96$, $p<0.001$), $y=0.11+0.92x$ ($r=0.94$, $p<0.001$), $y=0.0010+1.05x$ ($r=0.96$, $p<0.001$) and $y=0.00052+0.91x$ ($r=0.95$, $p<0.001$) for K_1, k_2, k_3 and K_i, respectively. The paired t test showed no significant difference between the methods. Differences were 2.5±19.9%, 0.5±18.1%, 1.9±15.7% and 0.6±11.2% for K_1, k_2, k_3 and K_i values, respectively.

The regression line equation for K_i values by Gjedde-Patlak analysis was $y=-0.00078+1.11x$ ($r=0.89$, $p<0.001$) and the paired t test showed no significant difference between the methods. The difference between the methods was 6.2±18.1%.

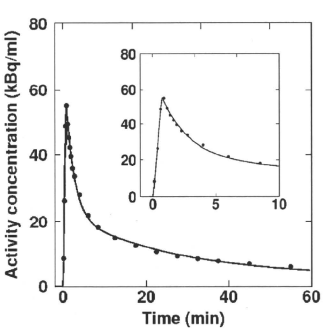

Fig. 5 TACs representing the mixed model input functions (Eq. 1), in comparison with the measured input function (*black circles*), generated by mixing the arterial and portal blood activity curves. The *inset* shows the input functions in the early phase

Discussion

In the current work, we validated a method to extract the mixed input function from liver [^{18}F]FDG PET images in experimental pig studies. The validity was shown in its coherence with measured input functions and in the tight correlation of hepatic glucose fractional extraction rate constant values between the present non-invasive method and the invasive blood sampling method. The results presented demonstrate that the input function can be estimated directly from PET images, supporting the fully non-invasive assessment of liver glucose metabolism in clinical applications. The perspective application attainable here is dual. On the one side, the comparison between measured arterial and estimated dual (arterial + portal) tracer levels provides indirect information on gut metabolism, and the gastrointestinal system is a metabolically active organ, manipulating ingested substrates and regulating their absorption. This apparatus is generally difficult to sample during imaging, due to its sparse location and thin walls, and the current approach could be used similar to a

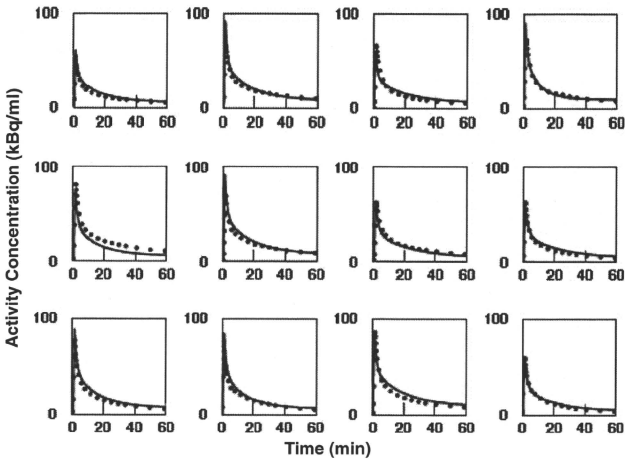

Fig. 6 Estimated input functions from PET images and their comparison with measured input (plot) functions

non-invasive arterial-venous balance through the organ. On the other side, the liver controls blood substrate levels, and its glucose uptake and phosphorylation appear to serve as signals for hepatic glucose release, also participating in the modulation of liver fatty acid and triglyceride metabolism. Thus, the assessment of HGU may be a target process in the pathogenesis and treatment of diabetes, dyslipidaemia and the metabolic syndrome.

The current approach estimated the hepatic input function from multiple tissue curves to calculate organ glucose uptake. A high degree of overlap and tight correlations were observed between the estimated input functions and those obtained by the blood sampling/counting during PET scans. Consequently, calculated rate constant values were consistent between the methods. The present approach was originally developed for hepatic perfusion studies with $H_2{}^{15}O$ PET [17], in which we documented optimal agreement between the estimated input functions and those obtained by the blood sampling/counting during PET scans, and between hepatic perfusion by PET and by ultrasonography. In our previous report, the arterial and portal inputs as well as the corresponding blood flow values were estimated separately because water could be assumed to be freely diffusible in the gut system and the variation in gut uptake rate constant was small enough to allow substitution of individual values with a fixed one. Thus, we could express the portal input uniquely from arterial input. In contrast, the extraction fraction of the current tracer ranged from 0.05 to 0.20 (*data not shown*) and the uptake rate constant value of [^{18}F]FDG in the gut system ranged from 0.20 to 0.80 min^{-1}, which cannot be replaced by an assumed common value. Furthermore, because the extraction fraction in the gut system is not 100%, and the shape of the arterial component flowing into the portal input and not being extracted could be assumed to be very similar to that of the arterial input, it is not feasible to distinguish the two contributions in mathematical formulations. Thus, the present method provides directly and solely a mixed input function.

As an alternative to the present procedure, a ROI-based input extraction from PET images has been used for the carotid artery in [^{11}C]flumazenil brain studies [24], the abdominal artery for kidney blood flow quantification with $H_2{}^{15}O$ [14], the aorta for cardiac [^{18}F]FDG metabolism [25] and for tumour blood flow using $H_2{}^{15}O$ [28]. In these approaches, ROIs are drawn in visible vessels and partial volume correction is needed; their application to HGU estimation is limited by the difficulty in identifying the portal vein in PET images. Closer to the current analysis, Di Bella et al. applied multiple tissue curves to estimate quantitative kinetic parameters in the brain [3], and reproduced the input function well for $H_2{}^{15}O$, showing the possibility to extract the input function from multiple tissue TACs, by assuming a single-tissue compartment model and a negligible blood volume component. The applicability of their method to the present [^{18}F]FDG liver study, which requires a two-tissue compartment model accounting for a large blood volume of 0.3 ml/ml [13], is unknown. Also, Sanabria-Bohórquez et al. [24] applied simultaneous fitting of multiple tissue TACs based on a

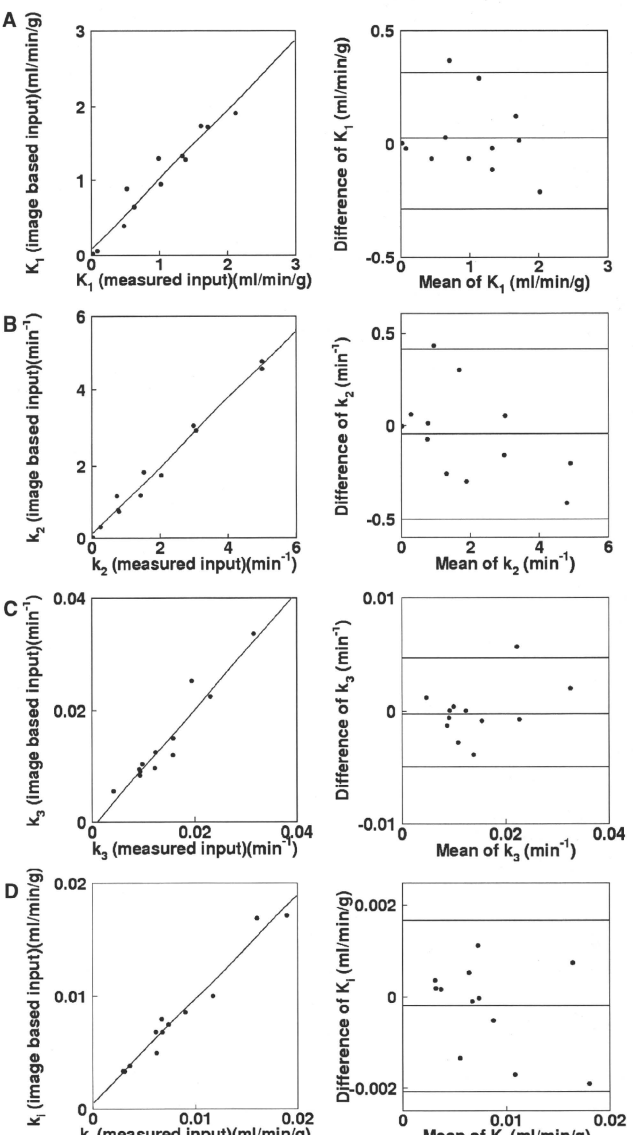

Fig. 7 Relationship (*left*) and Bland-Altman plot (*right*) between K_1 (**a**), k_2 (**b**), k_3 (**c**) and K_i (**d**) values, as estimated with measured and image-derived input functions. The *solid line* in *left figures* shows the regression line obtained, i.e. $y=0.09+0.93x$ ($r=0.96$, $p<0.001$), $y=0.11+0.92x$ ($r=0.94$, $p<0.001$), $y=0.0010+1.05x$ ($r=0.96$, $p<0.001$) and $y=0.00052+0.91x$ ($r=0.95$, $p<0.001$), for K_1, k_2, k_3 and K_i, respectively

mathematical description of a model input function similar to the present method and reproduced the input function well for [^{11}C]flumazenil. The method cannot be applied to HGU studies, because the formulae for the input function are partially based on the shape of image-derived curves from ROIs on visible carotid arteries. Otherwise, the shape of an arterial input function from multiple tissue TACs has been well reproduced in brain [^{18}F]FDG or [^{11}C]MPDX studies, by using an independent component analysis-based method (extraction of the plasma TAC using independent component analysis, EPICA) [19, 20], still requiring one arterial blood sample. The combination of the latter and the current techniques may provide a further simplification and deserves investigation, since it would entail neither a model function nor direct blood measurements.

One advantage of introducing a model function was to shape the curve of the input function by imposing constraints on the parameters range. We expect no relevant limitation in the extension of the assumptions concerning the shape to other species, and in a majority of hepatic conditions. A drawback in the use of a model function, however, is that the feasibility is unknown for a group in which the shape of input functions could be extremely different or cannot be expressed by the present model function. In this situation, the present method would require and may still be adapted to the use of group-specific parameter constraints or a modified model function. The present model function (Eq. 1) was created by assuming tracer bidirectional diffusion as well as metabolism in the whole body. The input functions obtained in the present study using this formula reproduced both the shape of measured inputs at the peak and the rate constant parameters well. In this study, the first 60-min data were used in the analysis, because most previous studies for quantification of HGU were performed using this scan duration (40 min: Iozzo et al. [11], 63 min: Choi et al. [4]). When the input functions were estimated using longer time data, the estimated input functions were almost superimposable until 90–120 min but they were higher thereafter; namely, only two input functions were overestimated by 5 and 10% for 90- and 120-min data, respectively, whereas a majority of input functions were overestimated, though still by 5–10%, for 180-min data. When estimation was limited to 40-min data, the height of the peak was 10–30% lower than that of measured input in three cases.

We considered the possibility to apply standardized input function methods, which assume that input function across subjects and conditions have an identical shape so that only a scaling factor is needed, which could be derived from the assessment of tracer concentrations in one or two blood samples. However, the input function shape varied depending on the injection procedure and the individual physiology of study animals. In fact, both the shapes and the scales were different (Fig. 6) among the weight-matched subjects used in the present study.

The present estimation procedure followed two steps, as designed to fit tissue curves individually and then simultaneously. The first step allowed careful exclusion of tissue TACs showing t_1 or t_2 values over one standard deviation from the mean, to eliminate the influence of radioactivity outside the liver region. In fact, in the experimental procedure, [^{18}F]FDG was injected into the femoral vein, draining into the vena cava, and the tracer was expected to show an early peak in the case of an anatomical overlap with the vena cava. The second step was introduced to facilitate the achievement of the convergence, by fixing the values of t_1, t_2, α and K_M to their calculated means (as shown in the simulation study, those parameters were less divergent than the remaining two parameters) to estimate the remaining two parameters. The shapes of input functions were reproduced and rate constant parameters of K_1, k_2, k_3 and K_i were consistent with those obtained by using measured inputs. Thus, the correlation among parameters, which may limit the identification of unique solutions due to local minima, did not seem to affect the estimation of HGU, though further study is required for optimization.

Although a close agreement was shown between estimated and measured input functions (Fig. 6), some modelled input functions showed over- and underestimations as compared to the measured ones, and the difference of the AUC was −3.6±8.0%, ranging from −10.8 to 12.3% between them. On the one side, this may be due to a model function-related error. On the other side, the difference may also be partly explained by inherent ultrasonography measurement error [from multiple measurements of flow data, the coefficient of variation was 13±5% for portal flow and 18±10% for hepatic arterial flow in this study (*data not shown*)], since ultrasonography defined the % hepatic input contributions from arterial and portal blood to construct the mixed input TAC from the measured data. However, we found tight correlations in rate constant values of K_1, k_2, k_3 and K_i (r=0.96, 0.94, 0.96 and 0.95, respectively, and p<0.001 for all), as computed by non-linear fitting assuming a two-tissue compartment model. There are two mathematical approaches used to quantify liver [^{18}F]FDG uptake and phosphorylation, i.e. graphical analysis [11, 18] and two-tissue compartment model [4, 11, 12, 18], the latter accounting for the potential dephosphorylation of [^{18}F]FDG-6-phosphate ([^{18}F]FDG-6P) occurring in hepatocytes. Both provide an estimation of a composite parameter (i.e. the fractional extraction of the tracer) intended as a unidirectional influx rate constant, which can be used to compute HGU once the lumped constant (LC) is known. Further studies are required to

compare quantitative accuracy obtained by different models by using our image-derived input approach.

The validation of the current approach, as obtained in this study, is especially valuable in the liver for multiple reasons. First, the inaccessibility of the portal vein prevents its direct blood sampling in humans. Arterial blood can be obtained, but blood counting requires corrections for dispersion [8] and delay [5, 9, 15, 16, 23, 27], and cross-calibration between PET scanner and radioactivity counter, which are all potential sources of errors. Second, HGU can be compromised both as a consequence and a cause of hepatic disease and may become a prognostic indicator and useful marker during progression or treatment follow-up.

In conclusion, our results demonstrate that the concentration of [^{18}F]FDG reaching the liver as input function can be estimated directly from tissue TACs obtained through dynamic [^{18}F]FDG PET imaging. The calculated HGU values using estimated and measured input functions were similar.

Acknowledgments The authors thank the technical staff of the Turku PET Centre for the efforts and skills dedicated to this project. The study was conducted within the "Centre of Excellence in Molecular Imaging in Cardiovascular and Metabolic Research" supported by the Academy of Finland, University of Turku, Turku University Hospital and Abo Academy. This work is part of the project Hepatic and Adipose Tissue and Functions in the Metabolic Syndrome (HEPADIP), which is supported by the European Commission as an Integrated Project under the 6th Framework Programme (contract LSHMCT-2005-018734). The study was further supported by grants from the Finnish Diabetes Foundation (P.I.), EFSD/Eli-Lilly (P.I.), Sigrid Juselius Foundation (N.K.), and Novo Nordisk Foundation (P.N.).

Appendix

A model function for hepatic input function for ^{18}FDG was created, by assuming a three-compartment model, in which the tracer is administered in a rectangular form and diffuses bidirectionally between arterial blood and whole-body peripheral tissue compartments. Part of the tracer is metabolized and accumulated in the third compartment. Differential equations for the model function ($C_I(t)$) can be expressed as;

$$\frac{dC_I(t)}{dt} = \frac{dF}{dt} - K_E C_I(t) + K_I C_{WB}(t) \tag{5}$$

$$\frac{dC_{WB}(t)}{dt} = K_E C_I(t) - K_I C_{WB}(t) - K_M C_{WB}(t) \tag{6}$$

$$\frac{dF}{dt} = \begin{matrix} A & (t_1 \le t \le t_2) \\ 0 & (elsewhere) \end{matrix} \tag{7}$$

where t_1 assumes the appearance time of administered tracer and t_2-t_1 represents the administration duration, A is scalar of input function. The equation F (Eq. 7) represents the bolus administration of tracer in the rectangular form with duration t_2-t_1. $C_{WB}(t)$ is the expected tracer concentration in whole-body peripheral tissues, K_E and K_I are bidirectional tracer diffusion rates between blood and peripheral tissue compartments, respectively, and K_M is the metabolic rate of the tracer in assumed whole body. Solving Eq. 6 for C_{WB} gives:

$$C_{WB}(t) = K_e e^{-(KI+KM)\cdot t} \int_0^t C_I(\tau) e^{(KI+KM)\cdot \tau} d\tau \tag{8}$$

The sum of Eq. 5 and $a \times$ Eq. 6 generates:

$$\frac{d(C_I(t) + aC_{WB}(t))}{dt} = \frac{dF}{dt} + (a-1)K_E(C_I + aC_{WB}) \tag{9}$$

where

$$a = (K_I/K_E - 1 + K_M/K_E)/2 + \sqrt{K_I/K_E + (K_I/K_E - 1 + K_M/K_E)^2}\Big/4 \tag{10}$$

Thus,

$$C_I(t) + aC_{WB}(t) = \frac{dF}{dt} \otimes \exp(-(1-a)K_E t) \tag{11}$$

where $\otimes$ indicates convolution integral. Substitution of C_{WB} from Eq. 8 into Eq. 11 after multiplying $e^{(KI+KM)\cdot t}$ gives:

$$e^{(KI+KM)\cdot t} C_I(t) + aK_E \int_0^t C_I(\tau) e^{(KI+KM)\cdot \tau} d\tau = e^{-(1-a)Ke\cdot t + (KI+KM)\cdot t} \int_0^t \frac{dF}{dt} e^{(1-a)Ke\cdot t} d\tau \tag{12}$$

Differentiation with respect to t after arrangement gives:

$$\left(\frac{K_I}{a} + K_E\right) C_I(t) + \frac{dC_I(t)}{dt} = \frac{K_I}{a} e^{-(1-a)Ke\cdot t} \int_0^t \frac{dF}{dt} e^{(1-a)Ke\cdot t} d\tau + \frac{dF}{dt} \tag{13}$$

Thus,

$$C_I(t) = \frac{K_I}{a} e^{-\beta \cdot t} \int_0^t e^{Ke \cdot (a-1) \cdot T + \beta \cdot T} \int_0^T \frac{dF}{dt} e^{Ke \cdot (1-a) \cdot \tau} d\tau dT + e^{-\beta \cdot t} \int_0^T \frac{dF}{dt} e^{Ke \cdot \beta \cdot \tau} d\tau \quad (14)$$

where $\beta = (K_I/a + K_E)$. Solving Eq. 14, we obtain:

$$C_1(t) = \begin{cases} 0. & (t < t_1) \\ A\left[\frac{1-\exp(\beta(t_1-t))}{\beta} + \frac{\alpha(1-\exp(\beta(t_1-t)))}{a(1-a)\beta} - \frac{\alpha(\exp(K_E(1-a)(t_1-t_2))-\exp(\beta(t_1-t)))}{a(1-a)\gamma}\right] & (t_1 < t < t_2) \\ \left[A\frac{\exp(\beta(t_2-t))-\exp(\beta(t_1-t))}{\beta} + \frac{\alpha(1-\exp(\beta(t_1-t_2)))}{a(1-a)\beta} + \frac{\alpha(\exp(K_E\beta(t_1-t_2))-\exp(\beta(t_1-t_2)))}{a(1-a)\gamma} \right. \\ \left. + \frac{\alpha(\exp(K_E(1-a)t_2)-\exp(K_E(1-a)t_1))(\exp(K_E(1-a)t)-\exp(\gamma t_2-\beta t)))}{a(1-a)\gamma}\right] & (t > t_2) \end{cases} \quad (15)$$

where $\alpha = K_I/K_E$ and $\gamma = (K_I/a + aK_E)$.

References

1. Alenius S, Ruotsalainen U. Bayesian image reconstruction for emission tomography based on median root prior. Eur J Nucl Med 1997;24:258–65.
2. Basu A, Basu R, Shah P, Vella A, Johnson CM, Nair KS, et al. Effects of type 2 diabetes on the ability of insulin and glucose to regulate splanchnic and muscle glucose metabolism: evidence for a defect in hepatic glucokinase activity. Diabetes 2000;49: 272–83.
3. Di Bella EV, Clackdoyle R, Gullberg GT. (1999) Blind estimation of compartmental model parameters. Phys Med Biol 1999;44: 765–80.
4. Choi Y, Hawkins RA, Huang SC, Brunken RC, Hoh CK, Messa C, et al. Evaluation of the effect of glucose ingestion and kinetic model configurations of FDG in the normal liver. J Nucl Med 1994;35:818–23.
5. Eriksson L, Kanno I. Blood sampling devices and measurements. Med Prog Technol 1991;17:249–57.
6. Ferre T, Riu E, Franckhauser S, Agudo J, Bosch F. Long-term overexpression of glucokinase in the liver of transgenic mice leads to insulin resistance. Diabetologia 2003;46:1662–8.
7. Gjedde A. Calculation of cerebral glucose phosphorylation from brain uptake of glucose analogs in vivo: a re-examination. Brain Res 1982;257:237–74.
8. Iida H, Kanno I, Miura S, Murakami M, Takahashi K, Uemura K. Error analysis of a quantitative cerebral blood flow measurement using H2(15)O autoradiography and positron emission tomography, with respect to the dispersion of the input function. J Cereb Blood Flow Metab 1986;6:536–45.
9. Iida H, Higano S, Tomura N, Shishido F, Kanno I, Miura S, et al. Evaluation of regional differences of tracer appearance time in cerebral tissues using [15O] water and dynamic positron emission tomography. J Cereb Blood Flow Metab 1988;8:285–8.
10. Iozzo P, Hallsten K, Oikonen V, Virtanen KA, Kemppainen J, Solin O, et al. Insulin-mediated hepatic glucose uptake is impaired in type 2 diabetes: evidence for a relationship with glycemic control. J Clin Endocrinol Metab 2003;88:2055–60.
11. Iozzo P, Geisler F, Oikonen V, Maki M, Takala T, Solin O, et al. Insulin stimulates liver glucose uptake in humans: an 18F-FDG PET Study. J Nucl Med 2003;44:682–9.
12. Iozzo P, Gastaldelli A, Järvisalo MJ, Kiss J, Borra R, Buzzigoli E, et al. 18F-FDG assessment of glucose disposal and production rates during fasting and insulin stimulation: a validation study. J Nucl Med 2006;47:1016–22.
13. Iozzo P, Jarvisalo MJ, Kiss J, Borra R, Naum GA, Viljanen A, et al. Quantification of liver glucose metabolism by positron emission tomography: validation study in pigs. Gastroenterology 2007;132:531–42.
14. Juillard L, Janier M, Fouque D, Lionnet M, Le Bars D, Cinotti L, et al. Renal blood flow measurement by positron emission tomography using 15O-labeled water. Kidney Int 2000;57: 2511–8.
15. Kanno I, Iida H, Miura S, Murakami M, Takahashi K, Sasaki H, et al. A system for cerebral blood flow measurement using an H215O autoradiographic method and positron emission tomography. J Cereb Blood Flow Metab 1987;7:143–53.
16. Kudomi N, Choi E, Watabe H, Kim KM, Shidahara M, Ogawa M, et al. Development of a GSO detector assembly for a continuous blood sampling system. IEEE Trans Nucl Sci 2003;50:70–73.
17. Kudomi N, Slimani L, Järvisalo MJ, Kiss J, Lautamäki R, Naum GA, et al. Non-invasive estimation of hepatic blood perfusion from H2 15O PET images using tissue-derived arterial and portal input functions. Eur J Nucl Med Mol Imaging 2008;35: 1899–911.
18. Munk OL, Bass L, Roelsgaard K, Bender D, Hansen SB, Keiding S. Liver kinetics of glucose analogs measured in pigs by PET: importance of dual-input blood sampling. J Nucl Med 2001;42: 795–801.
19. Naganawa M, Kimura Y, Nariai T, Ishii K, Oda K, Manabe Y, et al. Omission of serial arterial blood sampling in neuroreceptor imaging with independent component analysis. Neuroimage 2005;26:885–90.
20. Naganawa M, Kimura Y, Ishii K, Oda K, Ishiwata K, Matani A. Extraction of a plasma time-activity curve from dynamic brain PET images based on independent component analysis. IEEE Trans Biomed Eng 2005;52:201–10.
21. Patlak CS, Blasberg RG, Fenstermacher JD. Graphical evaluation of blood-to-brain transfer constants from multiple-time uptake data. J Cereb Blood Flow Metab 1983;3:1–7.

22. Patlak CS, Blasberg RG. Graphical evaluation of blood-to-brain transfer constants from multiple-time uptake data. Generalizations. J Cereb Blood Flow Metab 1985;5:584–90.
23. Ruotsalainen U, Raitakari M, Nuutila P, Oikonen V, Sipilä H, Teräs M, et al. Quantitative blood flow measurement of skeletal muscle using oxygen-15-water and PET. J Nucl Med 1997;38: 314–9.
24. Sanabria-Bohórquez SM, Maes A, Dupont P, Bormans G, de Groot T, Coimbra A, et al. Image-derived input function for [11C]flumazenil kinetic analysis in human brain. Mol Imaging Biol 2003;5:72–8.
25. van der Weerdt A, Klein LJ, Boellaard R, Visser CA, Visser FC, Lammertsma AA. Image-derived input functions for determination of MRGlu in cardiac (18)F-FDG PET scans. J Nucl Med 2001;42:1622–9.
26. Varga J, Szabo Z. Modified regression model for the Logan plot. J Cereb Blood Flow Metab 2002;22:240–4.
27. Votaw JR, Shulman SD. Performance evaluation of the Pico-Count flow-through detector for use in cerebral blood flow PET studies. J Nucl Med 1998;39:509–15.
28. Watabe H, Channing MA, Riddell C, Jousse F, Libutti SK, Carrasquillo JA, et al. Noninvasive estimation of the aorta input function for measurement of tumor blood flow with. IEEE Trans Med Imaging 2001;20:164–74.

Hyperintense Plaque With Noncontrast T1-Weighted Magnetic Resonance Coronary Plaque Imaging Leading to Acute Coronary Syndrome

Atsushi Tanaka, MD; Tomohiro Kawasaki, MD; Teruo Noguchi, MD; Shoichi Koga, MD; Yoshihiro Hiramatsu, MD; Takaya Fukuyama, MD; Nobuhiko Koga, MD

A 73-year-old diabetic man underwent multislice computed tomography (MSCT) and noncontrast T1-weighted (T1W) magnetic resonance imaging (MRI) for the evaluation of atypical chest discomfort after an exercise ECG was nondiagnostic. The MSCT demonstrated a low-density positive remodeling plaque and spotty calcification without significant stenosis in the proximal segment of the right coronary artery (Figure 1A and 1B). Noncontrast T1W MRI, using a 1.5-T MR system (Intera, Philips Medical Systems, Best, the Netherlands), revealed a hyperintense plaque (HIP) in the right coronary artery in an area corresponding to the plaque visualized by MSCT (Figure 1C and 1D). With clear evidence of atherosclerotic disease, the patient

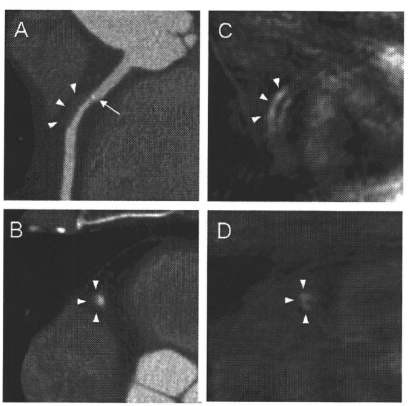

Figure 1. Multislice computed tomography (A, curved multiplanar reconstruction; B, horizontal) demonstrates low-density plaque (−36 Hounsfield units, remodeling index 1.6, arrowheads) with spotty calcification (arrow) in the proximal segment of the right coronary artery. On the corresponding noncontrast T1-weighted magnetic resonance imaging (C, oblique image; D, horizontal), this low-density plaque was visualized as a hyperintense lesion (arrowheads).

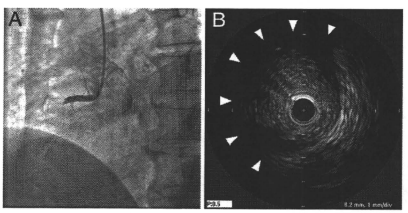

Figure 2. Right coronary angiography revealed an occlusion of the proximal segment of the right coronary artery (A). On intravascular ultrasound examination (B), a near-circumferential attenuation (arrowheads) was observed at the culprit lesion, corresponding with the plaque observed both by multislice computed tomography and by noncontrast T1-weighted magnetic resonance imaging.

was given glimepiride and voglibose with recommendations for strict diet therapy for treatment of diabetes mellitus; he continued to take aspirin. One year after these examinations, the patient presented with sudden-onset crushing chest pain at our emergency room. Despite the modifications to his medications, his coronary risk factors had not improved (hemoglobin A_{1c}, 7.1–6.4%, low-density lipoprotein cholesterol, 124–110 mg/dL; high-density lipoprotein cholesterol, 34–32 mg/dL). On admission, an ECG showed ST-segment elevation in leads II, III, and aV_F. Emergent coronary angiography revealed an obstructive lesion in the proximal segment of the right coronary artery in a region corresponding to the HIP previously identified by MRI (Figure 2A). Intravascular ultrasound confirmed extensive attenuation (Figure 2B) at that segment, and a bare metal stent was successfully implanted with a distal protection device. After stent implantation, a large amount of debris was collected.

Recently, Kawasaki et al[1] reported that the presence of HIP on noncontrast T1W MRI is associated with positive coronary remodeling, low CT density, and ultrasound attenuation by MSCT or intravascular ultrasound. However, it is unknown whether HIP has a greater potential for plaque rupture and subsequent acute coronary syndrome. To our knowledge,

From the Department of Cardiology, Koga Hospital 21, Kurume (A.T., S.K., Y.H.), Cardiovascular Center, Shin-Koga Hospital, Kurume (T.K., T.F., N.K.), and Division of Cardiology, Department of Medicine, National Cardiovascular Center, Suita (T.N.), Japan.

Correspondence to Tomohiro Kawasaki, MD, Cardiovascular Center, Shin-Koga Hospital, 120, Tenjin-cho, Kurume, 830–8577, Japan. E-mail to-kawasaki@mug.biglobe.ne.jp

(*Circulation.* **2009;120:2400-2401.**)

Circulation **is available at http://circ.ahajournals.org**

DOI: 10.1161/CIRCULATIONAHA.108.895482

this is the first report documenting the progression of HIP to acute coronary syndrome. Thus, HIP detected by noncontrast T1W MRI has the potential to identify vulnerable coronary lesions.

Disclosures

None.

Reference

1. Kawasaki T, Koga S, Koga N, Noguchi T, Tanaka H, Koga H, Serikawa T, Orita Y, Ikeda S, Mito T, Goto Y, Shintani Y, Tanaka A, Fukuyama T. Characterization of hyperintense plaque with non-contrast T1-weighted cardiovascular magnetic resonance coronary plaque imaging: comparison with multislice computed tomography and intravascular ultrasound. *J Am Coll Cardiol Cardiovasc Imaging*. 2009;6:720–728.

JACC: CARDIOVASCULAR IMAGING
© 2009 BY THE AMERICAN COLLEGE OF CARDIOLOGY FOUNDATION
PUBLISHED BY ELSEVIER INC.

VOL. 2, NO. 6, 2009
ISSN 1936-878X/09/$36.00
DOI:10.1016/j.jcmg.2009.01.016

Characterization of Hyperintense Plaque With Noncontrast T_1-Weighted Cardiac Magnetic Resonance Coronary Plaque Imaging

Comparison With Multislice Computed Tomography and Intravascular Ultrasound

Tomohiro Kawasaki, MD,* Shoichi Koga, MD,† Nobuhiko Koga, MD,*
Teruo Noguchi, MD,‡ Hidenori Tanaka, MD,* Hisashi Koga, MD,* Takeshi Serikawa, MD,*
Yoshiya Orita, MD,* Shinsuke Ikeda, MD,* Takahiro Mito, MD,* Yoshitaka Goto, MD,*
Yoshiaki Shintani, MD,* Atsushi Tanaka, MD,† Takaya Fukuyama, MD*
Kurume, and Suita, Japan

OBJECTIVES This study sought to characterize coronary hyperintense plaques (HIP) using noncontrast T_1-weighted imaging (T1WI) in cardiac magnetic resonance, which was then compared with multislice computed tomography and intravascular ultrasound.

BACKGROUND Carotid plaque components such as intraplaque hemorrhages and/or lipid-rich necrotic cores can be detected as HIP by noncontrast T1WI. Although coronary HIPs have been successfully detected using this technique, the properties of hyperintense signals in coronary plaques have not yet been systematically evaluated.

METHODS Thirty-eight lesions from 37 patients with angina pectoris who demonstrated >70% coronary stenosis on multislice computed tomography were evaluated by noncontrast T1WI using a 1.5-T magnetic resonance imager, and 25 lesions were evaluated by intravascular ultrasound. Signal intensity of coronary plaque to cardiac muscle ratio >1.0 was defined as HIP. We divided 25 lesions into the 2 groups, according to the presence or absence of HIP: HIP (n = 18) and non-HIP (n = 7) groups.

RESULTS In comparison with the non-HIP group, the HIP group demonstrated significantly higher coronary plaque to cardiac muscle ratio (1.7 ± 0.7 vs. 0.9 ± 0.1, $p < 0.01$), higher frequency of positive remodeling as observed by both multislice computed tomography (89% vs. 0%, $p<0.0001$) and intravascular ultrasound (94% vs. 14%, $p < 0.001$) and ultrasound attenuation (100% vs. 14.3%, $p < 0.0001$). The frequency of spotty calcification tended to be higher in HIP (89% vs. 50%, $p = 0.079$). The HIP group also exhibited a significantly lower computed tomography density (−23.2 ± 20.7 Hounsfield units [HU] vs. 9.6 ± 20.5 HU, $p < 0.01$). In addition, the incidence of transient slow-flow phenomena was significantly higher in the HIP group than in the non-HIP group (83% vs. 14%, $p < 0.01$).

CONCLUSIONS The typical HIP case was associated with ultrasound attenuation, positive remodeling, remarkably low computed tomography density, and a high incidence of slow-flow phenomena. Noncontrast T1WI in cardiac magnetic resonance imaging may be useful for the assessment of coronary plaque characterization in patients with coronary artery disease. (J Am Coll Cardiol Img 2009;2:720–8) © 2009 by the American College of Cardiology Foundation

From the *Cardiovascular Center, Shin-Koga Hospital, and †Department of Cardiology, Koga Hospital 21, Kurume, Japan; and the ‡Division of Cardiology, Department of Medicine, National Cardiovascular Center, Suita, Japan.

Manuscript received September 17, 2008; revised manuscript received January 6, 2009, accepted January 9, 2009.

Cardiac magnetic resonance (CMR) imaging (1–3) and multislice computed tomography (MSCT) (4–7) are attracting attention as new noninvasive imaging techniques for coronary plaque visualization. Noncontrast T_1-weighted imaging (T1WI) in CMR enables the identification of the thickened coronary wall (1–3). In addition, contrast-enhanced CMR allows us to identify areas of delayed enhancement that correlate with the severity of atherosclerosis as measured by MSCT and quantitative coronary angiography (8).

See page 729

In carotid plaques, high signals on inversion recovery-based 3-dimensional T1WI are associated with complicated plaques (type VI as proposed by the American Heart Association) (9) and with recent ischemic cerebrovascular events (10,11). Thus, CMR with T1WI is able to successfully identify vulnerable carotid plaques. Although coronary plaque imaging by noncontrast- and contrast-enhanced T1WI has been successfully demonstrated, and coronary plaques can be visualized as hyperintense signal areas, the properties of hyperintense signals in coronary plaques detected by T1WI have not yet been systematically evaluated.

To address this, we sought to characterize hyperintense coronary plaques visualized by noncontrast T1WI in CMR to compare findings obtained by MSCT and intravascular ultrasound (IVUS).

METHODS

Study population. Thirty-seven consecutive angina pectoris patients with a total of 38 lesions were enrolled. In all of these patients, significant coronary stenosis (>70%) was detected on MSCT; all were scheduled for elective percutaneous coronary intervention (PCI) between February 2007 and November 2007. All 38 lesions (37 patients) had been evaluated by noncontrast T1WI in CMR before PCI. Twenty-eight lesions from 27 patients contained areas with hyperintense signals, corresponding to the target lesions on MSCT (defined as hyperintense plaque [HIP]). In contrast, 10 lesions from the remaining 10 patients contained areas without hyperintense signals (defined as non-HIP). We excluded 13 lesions from 13 patients, 10 HIP and 3 non-HIP, who had not undergone IVUS examination during PCI. Thus, 25 lesions from 24 patients (18 HIP and 7 non-HIP) were examined in this study (Fig. 1). Both MSCT and CMR were performed within a month before the IVUS examination. The study protocol was approved by the Institutional Board on Clinical Investigations at Shin-Koga Hospital. Information regarding this study was provided either orally or in written form to all subjects, and written informed consent was obtained from each subject.

CMR coronary plaque imaging. Coronary plaque imaging was obtained with a 1.5-T MR imager (Intera, Philips Medical Systems, Best, the Netherlands) using 5-element cardiac coils. When heart rates were more than 65 beats/min, the rates were adjusted by administration of 20 to 40 mg of metoprolol 30 min before imaging. Nitroglycerin (0.3 mg) was also administered sublingually immediately before taking images to obtain high-quality CMR images. The survey images were focused around the heart, and the reference images were taken under free breathing to improve the sensitivity of parallel imaging. Coronary plaque images were obtained when patients were breathing freely, with the use of a 3-dimensional, T1W inversion-recovery gradient-echo sequence with fat-suppressed and radial k-space sampling (repetition time: shortest ≒ 4.7 ms, echo time: shortest ≒ 1.37 ms, flip angle: 20°, excitations per cardiac cycle: 15 to 45, SENSE factor: 2.5, number of excitations: 2, navigator gating window: 5 mm, no drift correction, field of view: 300 × 270 × 112 mm, acquisition matrices: 224 × 224, reconstruction matrices: 512 × 512 × 140). Spatial resolution was 1.34 × 1.34 × 1.6 mm. The same value was set for the acquisition window as in the coronary CMR. The acquisition window was set, according to the movement of the heart, for the time during the diastolic phase at which the heart moves the least. The movement of the heart was confirmed using cine-MR images that had been taken previously. The cine-MR images were obtained with a steady-state sequence as the patient was free breathing (repetition time: 2.6 ms, echo time: 1.3 ms, flip angle: 60°, field of view: 360 × 324 × 7 mm, acquisition matrix: 192 × 192, cardiac phases: 50, SENSE factor: 3.0, imaging time: 2 s).

A coronary CMR image analysis was performed by 2 technicians who were blinded to the plaque information obtained by MSCT. In the coronary CMR image obtained, if the areas that corre-

ABBREVIATIONS AND ACRONYMS

CMR = cardiac magnetic resonance
HIP = hyperintense plaque
IVUS = intravascular ultrasound
MSCT = multislice computed tomography
PCI = percutaneous coronary intervention
PMR = coronary plaque to cardiac muscle ratio
RI = remodeling index
T1WI = T_1-weighted imaging

JACC: CARDIOVASCULAR IMAGING, VOL. 2, NO. 6, 2009
JUNE 2009:720–8

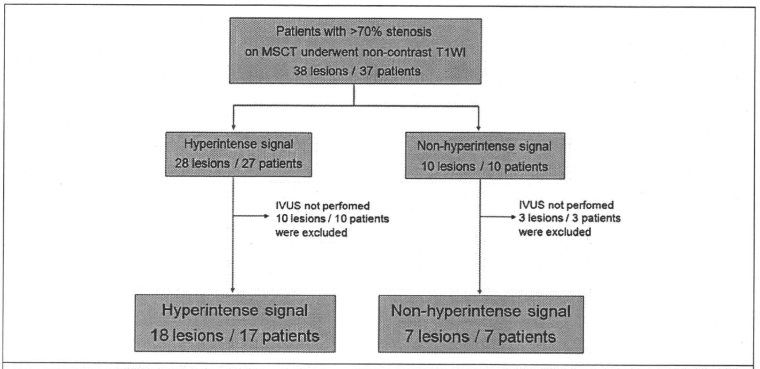

Figure 1. Flow Chart of Inclusion Criteria

A total 38 lesions from 37 patients with significant coronary stenosis (>70%) underwent noncontrast T1W cardiac magnetic resonance; overall, 24 patients (a total of 25 lesions; 18 lesions with hyperintense signal and 7 with nonhyperintense signal) were enrolled in this study. IVUS = intravascular ultrasound; MSCT = multislice computed tomography; T1WI = T_1-weighted image.

sponded to the target lesion on MSCT were confirmed, then the signal intensity of coronary plaque to muscle ratio (PMR) (PMR was defined as the signal intensity of the coronary plaque divided by the signal intensity of the cardiac muscle) was calculated. Areas with PMR >1.0 were defined as HIP, whereas areas with PMR ≤1.0 were defined as non-HIP. The representative cases with HIP and with non-HIP are shown in Figure 2. The signal intensity of the myocardium was measured at a site of the left ventricle near the coronary plaque.

Coronary Computed Tomography (CT) angiography. Coronary CT angiography was performed using MSCT (LightSpeed Volume CT, GE Healthcare, Milwaukee, Wisconsin). A coronary image was acquired with 64 × 0.625-mm slice collimation, a gantry rotation time of 0.35 ms, table feed: 7.2 to 8.2 mm/rotation, tube energy: 120 kV, and effective tube current: 280 mA. The total amount of contrast media (50.1 ± 5.1 ml iopamidol, 370 mgI/ml) (Schering AG, Berlin, Germany) was injected intravenously at a rate of 3.5 to 4.0ml/s. Transaxial images were reconstructed using a medium sharp conventional kernel/standard smooth kernel (B25F) and sharp kernel (B46F). The image matrix was 512 × 512 pixels, with a slice thickness of 0.75 mm and an increment of 0.4 mm using an electrocardiography-gated half-scan algorithm with a resulting temporal resolution of 165 ms in the center of rotation. Image reconstruction was retrospectively gated to the electrocardiogram. The patients with a heart rate >70 beats/min received 20 mg of metoprolol orally 60 min before scanning, and almost all of the patients received 0.3 mg of nitroglycerin sublingually just before scanning. Image reconstruction was performed using a 3-dimensional workstation (Advantage Workstation version 4.2, GE Healthcare). A focal multiplanar reconstruction image and cross-sectional image at the lesion were used for the assessment of coronary plaque morphology, including vessel remodeling index (RI), the minimum CT density of the plaques (expressed by Hounsfield units [HU]), and spotty calcification. The RI on MSCT was calculated by dividing the cross-sectional vessel area at the lesion by the mean of the 2 reference areas, which were obtained within 5 mm proximal to and 5 mm distal to the lesion. Positive remodeling was defined as RI >1.10 (12). Spotty calcification was defined as features <3 mm in size on a focal multiplanar reconstruction image and cross-sectional image in the lesion (13,14). An MSCT image analysis was performed by 2 technicians who were blinded to the plaque information obtained by CMR and IVUS.

IVUS image. The IVUS image was obtained before the PCI within 1 or 2 weeks after the CMR and MSCT. The IVUS system used a commercially available 40-MHz IVUS catheter (Atlantis Pro 2.9-F, Boston Scientific, Natick, Massachusetts) with 0.5 mm/s auto-pullback. The manual con-

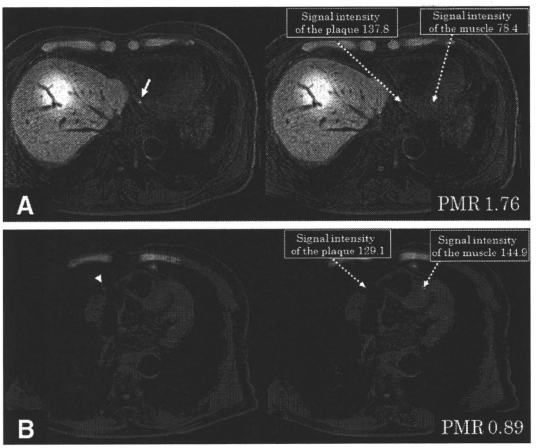

Figure 2. Representative Case With and Without HIP

(A) Representative case with hyperintense area **(white arrow)** at distal right coronary artery **(left panel)**. In this case, the intensity of coronary plaque to cardiac muscle ratio (PMR) was 1.76 and it was classified as a hyperintense plaque (HIP) **(right panel)**. **(B)** Representative case without hyperintense signal area **(arrowhead)** at proximal right coronary artery **(left panel)**. The PMR was 0.89 and it was classified as non-HIP **(right panel)**.

tour detection of the external elastic membrane was performed at the lesion and at the proximal reference site, and the RI was then calculated as the external elastic membrane of the lesion divided by the external elastic membrane of the proximal reference site, as previously described (15,16). Positive remodeling was defined as RI >1.05 (17). In addition, the plaque was checked to determine whether ultrasound attenuation was present. Ultrasound attenuation was defined as backward attenuation of signals behind the coronary atheroma without echogenic deposits or calcium within the plaque (18). The grade of ultrasound attenuation was classified into 3 categories according to the arc of the attenuation as follows: − = no attenuation; + = attenuation <180°; ++ = attenuation ≥180°(18).

Statistical analysis. Continuous data were summarized as mean ± SD. Categorical data were summarized as counts and percentages. The comparison of the plaque characteristics between the HIP and non-HIP groups was made using an unpaired *t* test in continuous data and Fisher exact tests in categorical data. All interpretations of CMR, MSCT, and IVUS imaging were performed in a blinded manner. Interobserver agreement was calculated using kappa statistics. A value of $p < 0.05$ was considered statistically significant.

RESULTS

Of all 25 lesions used in the study, 18 lesions (72%) were classified as HIP and 7 lesions (28%) were classified as non-HIP. The baseline characteristics of those 25 lesions (from 24 patients) are shown in Table 1. Other than in target coronary vessel involvement, there was no statistically significant difference in patient clinical characteristics between HIP and non-HIP lesions. The relationship between the HIP/non-HIP lesions on noncontrast T1WI and the plaque morphology obtained by MSCT and IVUS is shown in Table 2 and is summarized in Table 3. The averaged PMR in HIP lesions was significantly higher than in non-HIP lesions (1.70 ± 0.71 vs. 0.90 ± 0.08, $p < 0.001$). Positive remodeling on MSCT was observed in 16 (89%) of the 18 patients with HIP as opposed to 0 (0%) of the 7 patients with non-HIP. In addition, minimal CT density was significantly lower in HIP lesions (−23.2 ± 20.7 HU vs. 9.6 ± 20.5 HU, $p < 0.01$).